bioRχiv

Correlative MS Imaging for cellular identification and analysis of *in situ* cryo-ET

Andre Schwarz[a,#], Jakob Meier-Credo[a,b,#], Arne Behrens[c], Jürgen Reichert[b], Lea Dietrich[a], Erin M. Schuman[a], Julian D. Langer[a,b,*]
[a]Max Planck Institute for Brain Research; Frankfurt, 60438, Germany
[b]Max Planck Institute for Biophysics; Frankfurt, 60348, Germany
[c]Bruker Daltonics GmbH & Co KG; Bremen, 28359, Germany
*Correspondence should be addressed to J.D.L. (julian.langer@brain.mpg.de), #These authors contributed equally to this work

***In situ* cryo-electron tomography (cryo-ET) offers direct access to protein structures in their native state in cells. A central challenge for this technique comprises the identification and classification of the imaged cells, as sample heterogeneity and differences in cell types and functional states can significantly impact the data. Currently, tools to determine a cell's identity or state are limited to fluorescent labeling or subtomogram averaging, which require genetic modifications or rely on the availability of suitable dyes or identifiable and informative macromolecules. Here we present an integrated pipeline combining MALDI-MS Imaging (MSI) and *in situ* cryo-ET for single-cell identification and classification. Our approach enables MSI data acquisition directly from EM grids that were previously analyzed using cryo-ET, and allows unambiguous identification and classification of cell species and type. The method can be used on any eukaryotic single-cell cryo-ET sample without prior modification and takes less than 36 h for the entire workflow per grid, with significant potential for parallelization. We anticipate that this approach will transform the way that structural biologists approach cellular heterogeneity in cryo-ET, as cells can be identified and classified reliably post acquisition.**

Introduction

In situ cryo-electron tomography (cryo-ET) has revolutionized structural biology: structures of protein complexes are accessible in their native cellular environment both in cultured cells (Mahamid et al., Science, 2016) and tissue samples (Schaffer et al., Nature Methods, 2019, Schiøtz et al, 2024; Nguyen et al., 2024). This technique provides essential new insights into e.g. the molecular mechanism of anti-cancer drugs (Xing et al., Science, 2023), muscle fiber organization (Wang et al., 2021) and the first molecular description of new microorganisms (Rodrigues-Oliveira et al., 2023). A key challenge for this method is the unambiguous determination of the identity and the state of the cells from which protein structures are obtained. In environmental samples or primary cell cultures, in which multiple organisms or cell types are present, the identity of a cell of interest has to be inferred from cryo-EM data or correlative labeling techniques (Pierson et al., 2024; Fung et al., 2023). However, these methods can affect or impair sample quality, rely on availibility of suitable reagents, and often yield limited information. In addition, they all rely on reporting distributions of selected markers and, while offering sensitive and robust detection for a specific target, may not capture cellular heterogeneity or different functional states of cells. So even for comparatively homogenous samples, e.g. a cell line in culture, the specific metabolic state of a cell can remain unclear.

MALDI-MS data is routinely used to identify micro-organisms in clinical isolates. The small molecule, lipid and small protein signal patterns are highly characteristic and utilized in clinical "Biotyping", to classify medically-relevant pathogens based on their MALDI mass spectra signatures. At present, more than 500 strains of different human pathogens can be identified with clinical validation (99.9% ID success rate) and more than 2000 strains are available in reference databases (with >98.3 ID success rate). These data thus represent a powerful metric for tissue and cell identification and characterization.

While Biotyping is conducted on extracts and homogenized samples, MS Imaging investigates the spatial distribution of metabolites, lipids and small proteins in a sample with micrometer resolution, so individual cells can be identified and characterized reliably. Single cell MSI can be used to differentiate cell types in mixed cultures or tissues, and to characterize and differentiate their metabolic states (Rappez et al., Nature Methods, 2021). A recent study using a combination of immunolabeling-based cell classification and MS Imaging-based lipid profiling enabled the determination of specific lipid patterns for different neuronal cell types, determining lipid profiles of neurons and glia (astrocytes and oligodendrocytes, Asadian et al.,2025). Recent studies also used other mass spectrometry-based imaging techniques such as secondary-ion mass spectrometry (SIMS) to study cryo-ET samples (Ochner et al., 2025), using a prototype instrument that enables direct SIMS-imaging from cryo-ET grids. This approach offers complementary, high-resolution

spatial information on small, inorganic molecule distributions in the sample. However, biomolecules such as lipids, signaling molecules and peptides are not directly accessible using conventional SIMS.

Here we present a correlative workflow for cryo-ET analysis **(Figure 1A)**, utilizing high-resolution MALDI-MS imaging to analyze individual cells post structural analysis by their lipid and small molecule profile, to unambiguously identify and classify single cells by species and type.

Results

Adapter and workflow

We first set out to construct an adapter that enables MALDI-based acquisition on EM grids, allowing direct analysis after cryo-ET data acquisition **(Figure 1A)**.

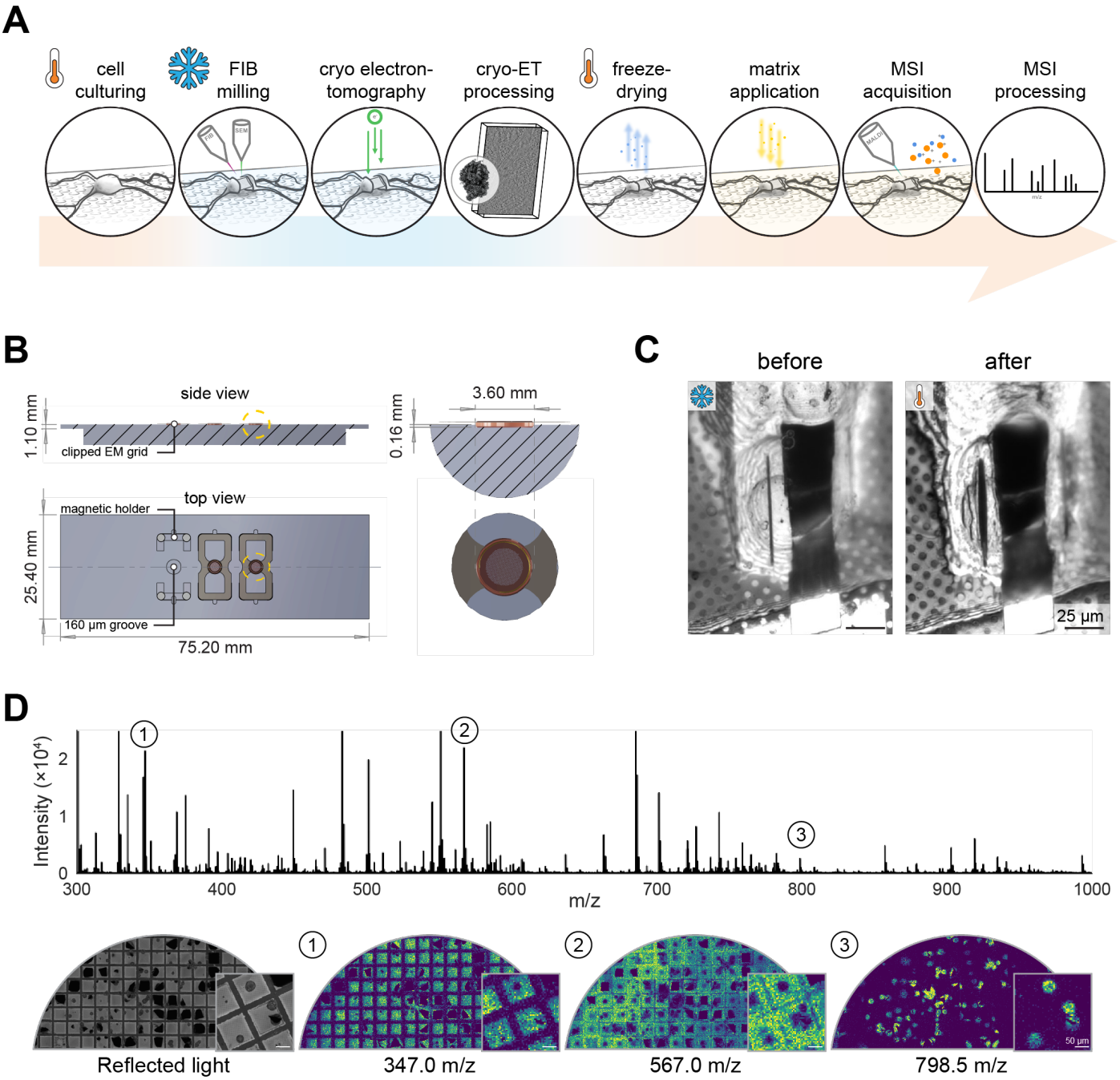

Figure 1: Correlative cellular cryo-ET and mass spectrometry imaging enables molecular profiling of plunge-frozen grids. (A) Schematic representation of correlative cellular cryo-electron tomography and mass spectrometry imaging workflow. **(B)** Technical drawing of custom built grid holder for mass spectrometry imaging of clipped cryo-EM grids. Grids are placed within a 160 μm indentation and held by metal springs via a magnetic holder to facilitate even imaging surface. **(C)** Reflected light images of a HeLa lamella before and after freeze-drying in a dual beam microscope. Gradual water sublimation leads to cell shrinkage visible by changing interference patterns. **(D)** Example m/z spectrum, individual m/z channel and reflected light images of an EM grid containing HeLa and Polytomella cells. Different m/z channels display specificity to background support, uniform signal across the grid, and cell-specific signal respectively. Y-axis is cropped at 2.5 X 10^4 for improved visibility.

Grids for cryo-ET are "clipped" into small holder rings for transfer within the electron microscope, so the plane of the grid and the cells is approximately 160 µm above the bottom edge of the clip rings. In order to fit grids directly into regular cover slide MALDI Imaging adapters, we designed and produced corrosion-resistant aluminium grid holder adapters using CAD and high-precision milling. Due to spatial limitations based on laser optics and instrument ion lenses, the adapter houses the EM grid in a recess secured by flat springs that attach to embedded magnets in the adapter base **(Figure 1B)**. To obtain data with high spatial resolution and a pixel size of 5 µm x 5 µm, we applied 2,5-Dihydroxybenzoic acid (DHB) matrix using a standard sublimation workflow. We then tested our adapters on Bruker Rapiflex and TimsTOF Flex instruments. We obtained robust and sensitive signals on both instruments. However, due to the grid clip ring and laser angle and coupling, we were only able to acquire data on the complete grid on the TimsTOF flex, with the rapifleX being limited to a central area of the EM grid.

We then tested and optimized drying methods for cryo-EM samples (e.g. cells grown or placed on EM grids). Conventional drying approaches led to cell rupturing and a loss of high resolution spatial information. We thus optimized gentle freeze-drying directly in the electron microscope **(Figure 1C, Figure S1)**, without any washing steps. This approach yielded grids with structures matching cell body positions prior to drying, with superior cellular anatomy and integrity **(Figure 1D)**. Notably, no significant, additional damage was observed to the carbon film on the grids during freeze-drying .

Cultured HeLa cells

Having established the sample preparation pipeline, we tested our approach on different model systems. First, we investigated if we could identify and assign HeLa cells grown on EM grids, dried in the EM stage and then prepared for MALDI-MS imaging using DHB sublimation. Overall, we detected multiple, clear signature peaks at the locations of cell bodies inferred from co-registered, optical images. These peaks matched known phospholipid components of the HeLa lipidome, which have been identified in multiple other studies previously. Specifically, we observed PC 34:1, PC 36:2 and PE 36:1 species with clear cellular localizations **(Figure S2)**, and annotated 73 phospholipid species in database searches in different preparations of HeLa cells grown on EM grids (**Table S1**). We then conducted on-grid MS/MS measurements of selected candidates, confirming the results of our database searches **(Figure S3A-B)**. In addition, we detected signals that were evenly distributed on the carbon film or enriched on grid bars, which are probably derived from dried medium, carbon support or grid coating (**Figure 1D**). Notably, the HeLa preparations tested here were stored for up to several years in liquid nitrogen prior to freeze-drying, and then several months in a desiccated environment between freeze-drying and MS Imaging analysis. We observed that cell size and shape differed between different preparations and cell batches. Also, we found different levels of cation adduct formation across these replicates. However, overall we identified identical phospholipid species across all experiments in similar quantities and distributions. We thus conclude that we can reliably and robustly detect and identify HeLa cells on EM support grids.

In order to holistically identify m/z channels that correspond to cell-specific molecules, we performed spatial cross-correlation analysis and hierarchical clustering **(Figure 2A, see methods)**. Most of the clusters corresponded either to "background" channels covering grid bars and/or the carbon support or were high noise channels without specific spatial pattern. Two clusters comprising 97 m/z channels however showed a clear enrichment for cells, as judged by correlated reflected light images **(Figure 2A, Table S2, Figure S4A)**. In order to investigated inter-cellular variability within our datasets, and whether we could discern distinct functional states in the cultured HeLa cells, we performed a second round of hierarchical clustering of these cell-specific m/z channels **(Figure 2B)**, identifying a cluster of m/z channels with strong correlation and signal-to-noise-ratio and several clusters of more variable channels with higher noise components. By correlating a reflected light-based mask for each cell **(Figure S4A)**, we next measured the mean intensity per area for each of the previously determined 97 cell-specific m/z channels. When viewed as a principle component analysis (PCA) of all cells across all m/z channels, a continuum emerged with cells at opposite ends exhibiting considerable variability for different m/z values **(Figure 2D)**. The most variable channel (PC 30:0 - 744.48 m/z, 284.9 $Å^2$) mirrored the largest axis of this variability along PC 1 and cells from opposite ends showed a strong difference in lipid content. When displayed alongside a more stable channel (PC 34:1 - 798.53 m/z, 293.1 $Å^2$), the increase in PC 30:0 was clearly noticeable in individual cells **(Figure 2E)**. This cellular heterogeneity is directly in line with previous MS Imaging studies on HeLa (Xi et al., 2020; Otsuka et al., 2025) and other cell lines in culture (Bien et al., 2022), showing cell-specific, distinct phospholipid profiles that displayed a certain degree of variation within their lipid composition.

We then examined if these signals were still detectable in cells that have been submitted to FIB-milling. For assignment and co-registration of MS Imaging and cryo-ET data, we made use of the regularly spaced grid pattern of the underlying electron microscopy supports, which is clearly visible in all electron- photon- and some mass spectrometry-imaging (m/z) channels. This underlying data structure enabled us to achieve high-accuracy co-registration of cryo-ET, optical and MSI data, even though the data is acquired at very different resolutions. This co-registration using a high number of evenly spaced reference points further allowed us to get a spatial estimate of the registration precision across the grid, ranging from 1.07 - 2.34 µm **(Figure S4B)** – less than half a pixel in MS Imaging. Sections with cut lamellae were clearly visible both in the optical and the MS Imaging data **(Figure 2F)**. Our primary datasets comprised cells that were milled across their cell bodies, i.e. the majority of the

cell volume was removed. We still observed clear lipid signals for most cells in the pixels adjacent to the milled volume, corresponding to the remaining cell density which is left for structural support of the lamella. These peaks include the main phospholipid species detected in unmilled cells, and clearly differ from the surrounding carbon film. These data demonstrate that we can identify milled cells and obtain quantitative information on their lipid composition.

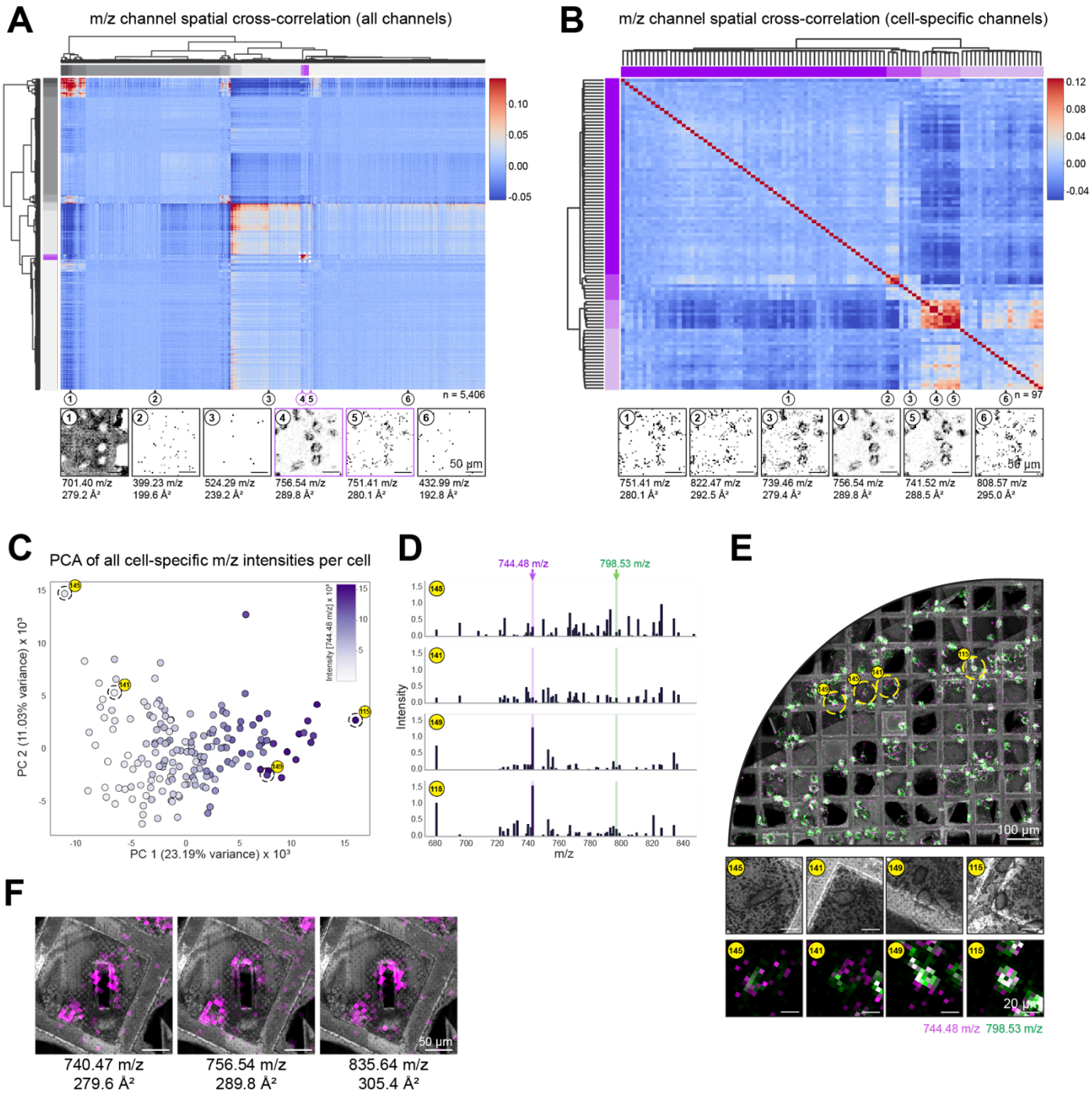

Figure 2: Mass spectrometry imaging of HeLa cells and lamellae shows significant variability between cells. (A) Hierarchical clustering of normalized spatial correlations to identify cell-specific m/z channels (n = 5,406). Example m/z channel images of selected clusters show prominent features of each cluster. Cell-specific clusters 9 and 10 are highlighted in purple. **(B)** Second round of hierarchical clustering of only cell specific channels from (A) (n = 97). Clusters 2-3 contain m/z channels with high signal-to-noise ratios, clusters 1, 4 show high noise components. **(C)** Principle component analysis of all individual cells over all cell-specific m/z channels in (B), colored by 744.48 m/z. A continuous distribution is observed with 744.48 m/z accounting for 65% of PC1. Individual cells along PC1 are highlighted. **(D)** Spectra for highlighted cells in (C) covering cell-specific m/z values from (B). X-axis is cropped to a lipid-rich region between 675 - 850. Shaded areas highlight variable m/z channel 744.48 (magenta) and stable channel 798.53 (green). **(E)** Reflected light overview of HeLa cells grown on an EM grid with overlaid m/z channels from (D). Individual cells from (C, D) are highlighted and enlarged. m/z channel 744.48 intensity (magenta) increases from cell #145 - #115. **(F)** Adjacent regions of cut lamellae retain clear MSI signal. Reflected light images and m/z channel overlays of channels showing enriched signal at regions adjacent to lamellae.

HeLa-*Polytomella* "species-mixing" experiment

We next investigated if the data we obtain in such an experiment are sufficient to identify and classify cells from different organisms. To this end, we conducted a "species-mixing" experiment using HeLa and *Polytomella* cells. *Polytomella* is a non-photosynthetic green alga which is significantly smaller than HeLa cells, but forms aggregates in solution leading to a wide range of clusters of varying size between 5 and 30 µm, and are thus difficult to distinguish from single HeLa cells. We prepared a set of grids in our cryo-ET workflow which contained only *Polytomella* cells, only HeLa cells, or a mixture of HeLa and *Polytomella* cells. We first examined the molecular distributions on our *Polytomella* grids and, using a co-localization analysis, found specific peaks matching the localization of *Polytomella* cells based on optical images. These peaks mainly correspond to different phospholipid species, which we matched to lipids detected in screening LC-MS lipidomics runs on *Polytomella* samples (list of matched lipids available in **Tables S3-4**). We then also conducted on-grid MS/MS measurements of selected candidates and confirmed the identifications using the respective fragment ion spectra **(Figure S3C-D)**. Taken together, we observed characteristic phospholipid species for *Polytomella* cells and cell clusters.

We then analyzed the grid containing a mixture of HeLa and *Polytomella* cells. As before, we conducted unsupervised clustering and segmentation analysis on the full MS Imaging datasets and found in total 89 peaks with cellular localization patterns forming two broad clusters **(Figure 3A, Figure S5, Table S5)**. The observed peak distributions are identical to the molecular species observed in previous experiments in HeLa cells grown on EM grids **(Table S2)**. We also found a second group of cells matching *Polytomella* signature phospholipid peaks and small molecule populations.

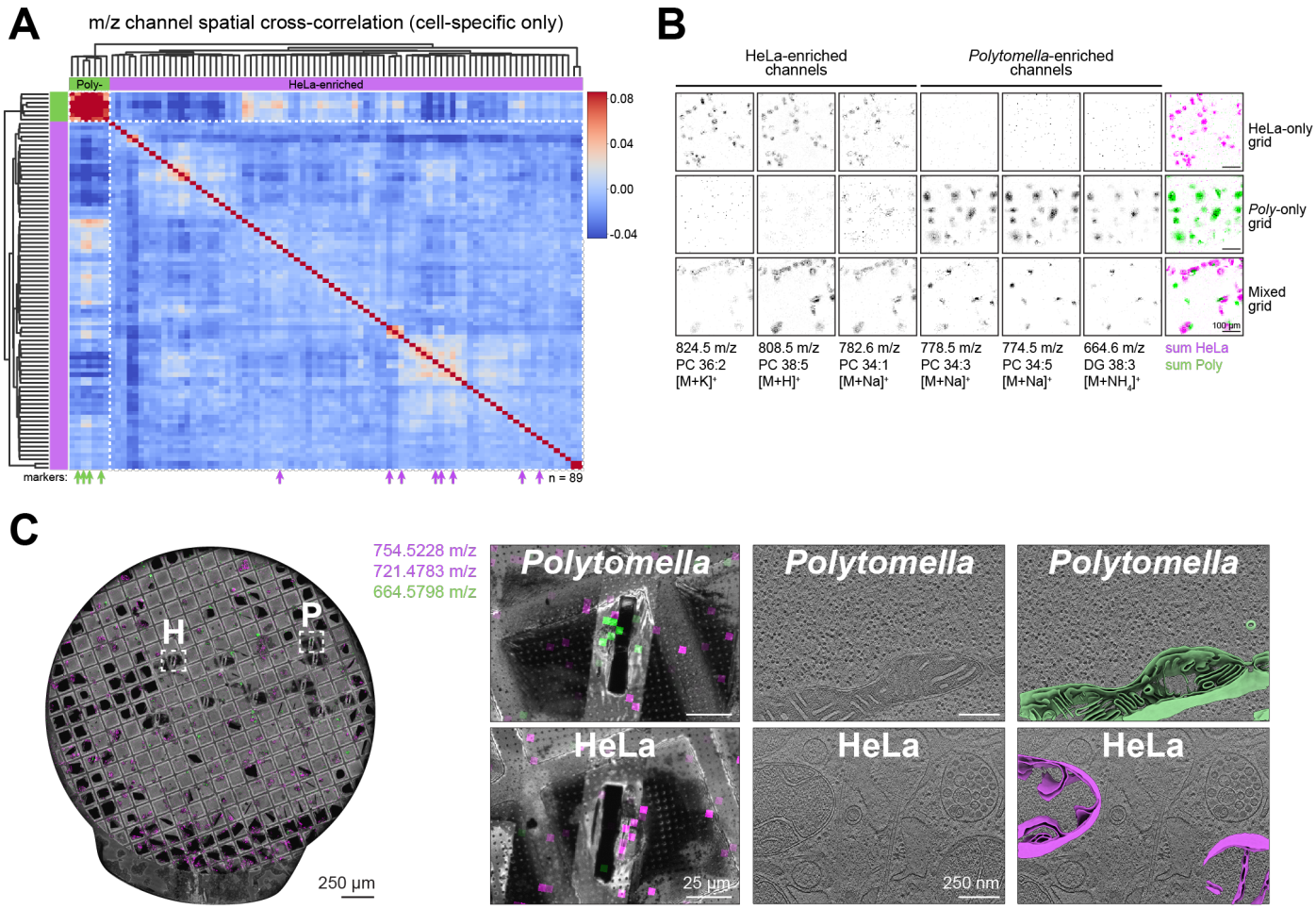

Figure 3: Mass spectrometry imaging signal can distinguish different species in mixed cryo-ET samples. (A) Hierarchical clustering of cell specific m/z channels from mixed HeLa / *Polytomella* grid (n=89) shows two prominent clusters. Marker channels identified on HeLa-only and *Polytomella*-only grids (magenta and green arrows) identify the clusters as *Polytomella*-enriched and HeLa-enriched m/z channels respectively. **(B)** Example m/z images from both clusters across HeLa-only, *Polytomella*-only, and mixed grids. Both sets of channels show clear spatial separation. **(C)** Reflected light overview of mixed HeLa / *Polytomella* grid with overlaid specific m/z channels from (A). Enlarged images of two lamellae with enriched *Polytomella*- or HeLa-enriched m/z channels with corresponding tomograms and segmentations acquired from these lamellae. Distinct and characteristic mitochondrial shapes confirm the molecular identification.

Using unsupervised clustering and segmentation analysis, we found that the signals in the HeLa and *Polytomella* cells clearly segregated into two distinct groups **(Figure 3A).** Individual marker channels identified on the *Polytomella*-only and HeLa-only grids **(Figure 3A**, green and magenta arrows) served to identify the clusters as *Polytomella*-enriched and HeLa-enriched m/z channels. These signature channels comprise mainly phospholipids such as PC 34:1 (HeLa) and PC 34:5 (*Polytomella*), which we previously identified as enriched markers for HeLa or *Polytomella* cells **(Figure 3B)**.

We next investigated if the remaining densities of FIB-milled cells provide MS Imaging data of sufficient quality for unambiguous assignment of HeLa and *Polytomella* cells. Based on the signature m/z channels identified in our unsupervised clustering, we were able to identify the cells at 7 out of 10 lamellae cut on the mixed grid . This classification was possible even though the lamellae were cut from the center of the cells, and the remaining densities often comprised less than 20 MSI pixels. It's worth noting that MSI intensities were generally lower in areas where cells were viewed and cut extensively with the scanning EM (SEM) and focused ion beams, hence some cells did not have enough signal left for unambiguous identification.

In order to evaluate our MSI-based classification, we next examined the cryo-ET data recorded from these lamellae. The tomograms often allow unambiguous assignment of the two cell types, as *Polytomella* cells contain mitochondria with characteristic, regularly stacked cristae clearly distinguishable from the tighter and less regularly stacked cristae in HeLa cells (Dietrich et al., 2024, Medina et al., 2025). The cryo-ET-based classification matched the MSI-based classification for all lamellae for which we obtained good tomograms **(Figure 3C)**, demonstrating that MS Imaging can be used to identify and classify single cells on EM grids after cryo-ET sample preparation and data acquisition.

Primary neuron cultures

We then examined primary cultured rat neurons grown on EM grids. These preparations represent a challenging sample as they contain multiple cell types (neurons and glia cells) and neurons form dense networks with extensive processes (axons and dendrites, collectively called "neurites"). Prior fluorescent imaging using NeuO, a neuron-specific fluorescent dye, enabled us to identify neuronal cell body positions on the EM grid and match structures visible in optical images **(Figure 4A)**. We found clearly distinguishable phospholipid peaks, with multiple phospholipids assigned using high-resolution MS and ion mobility data acquired on a TimsTOF instrument **(Table S6)**. We again confirmed our database matches by acquiring MS/MS data on selected candidates **(Figure S3E-F)**. Notably, cell body structures were larger and more diffuse than for HeLa cells and neuronal cell density significantly varied on grids and between different preparations. We attribute these observations to the complex morphology of neuronal cells, with extensive processes that form a dense network and their close proximity to other cells. The main lipid species identified in these samples also comprise major constituents of the neuronal lipidome (Asadian et al., 2025). Unsupervised clustering and segmentation analyses of our datasets also revealed 79 m/z channels matching cellular locations and specific phospholipid intensity distributions **(Table S7)**. Taken together, we conclude that we can reliably identify and trace neuronal cell bodies based on their phospholipid signatures.

We then investigated if we could, also here, obtain data from cell bodies that were submitted to FIB-milling. Notably, again, the lamellae were cut from the cells of interest in such a way that the majority of the cell body was removed **(Figure 4A)**. The areas directly surrounding these milled segments displayed characteristic changes, with a moderate signal reduction in some channels and a distinct signal increase in other channels **(Figure S6B)**. We speculate that these changes could be due to radiation damage during the FIB-milling process. However, cellular classification was not compromised as the affected channels were not cell-specific channels. We observed different phospholipid species in the respective neuronal cell body area and processes **(Figure 4A**), including PC species with varying degrees of saturation. As a proof of concept for the full workflow, we evaluated and analyzed the cryo-ET data from this grid, resulting in a 7.0 Å global resolution subtomogram average structure of ~15,000 rat neuronal ribosomes **(Figure 4B-C)**.

Primary hippocampal neuron preparations from brain tissue contain multiple cell types such as neurons and glia. We thus investigated if we could identify and discern these different cell populations in our MS Imaging data. We acquired MS Imaging data and conducted unsupervised hierarchical spatial correlation clustering on previously acquired and analyzed rat hippocampal grids (Manuscript submitted) that have been stored in liquid nitrogen for over two years between tilt series and MSI data acquisitions. Broadly, the clustering of cell-specific m/z channels **(Figure S6A)** resulted in an early split of three prominent clusters **(Figure 4C)**. In order to test whether any of these corresponded to specific cell types, we used a recently published fluorescence-guided single-cell MSI dataset matching lipids to individual brain-derived cell types via antibody staining (Asadian et al., 2025) as ground truth. When we queried neuron-enriched vs glia-enriched m/z channels, we indeed noticed that they separated into two of these clusters **(Figure 4D, green and magenta arrows, Figure S6C)**

Having established that we can distinguish neuron- vs glia-enriched m/z profiles on our mixed primary brain culture grids, we next wondered whether any of these cell-specific channels displayed any preferential spatial partitioning between cell bodies and the thin neuronal outgrowths collectively called neurites (i.e. axons and dendrites). In order to assess this, we utilized the previously acquired fluorescence microscopy images of NeuO to create masks for cell bodies (somata) and neurites **(Figure S6E, see methods for details)** with a target registration error to the MSI channels of 0.9 - 2.5 μm (Fig S6D). We then measured the mean intensity for each cell-specific m/z channel for these two compartments and noticed a wide range of partitioning, ranging

from channels with a ~2.5x enrichment in somata (e.g. 804.5481 m/z [PC 36:4], **Figure 4E**) to roughly even distributions (e.g. 756.5456 m/z [PC 34:3], **Figure 4E**). We conclude that we can still detect lipid distributions in neuronal processes even though their volumes and associated signal intensities are significantly lower than for somata, and that these lipids display distinct subcellular distributions.

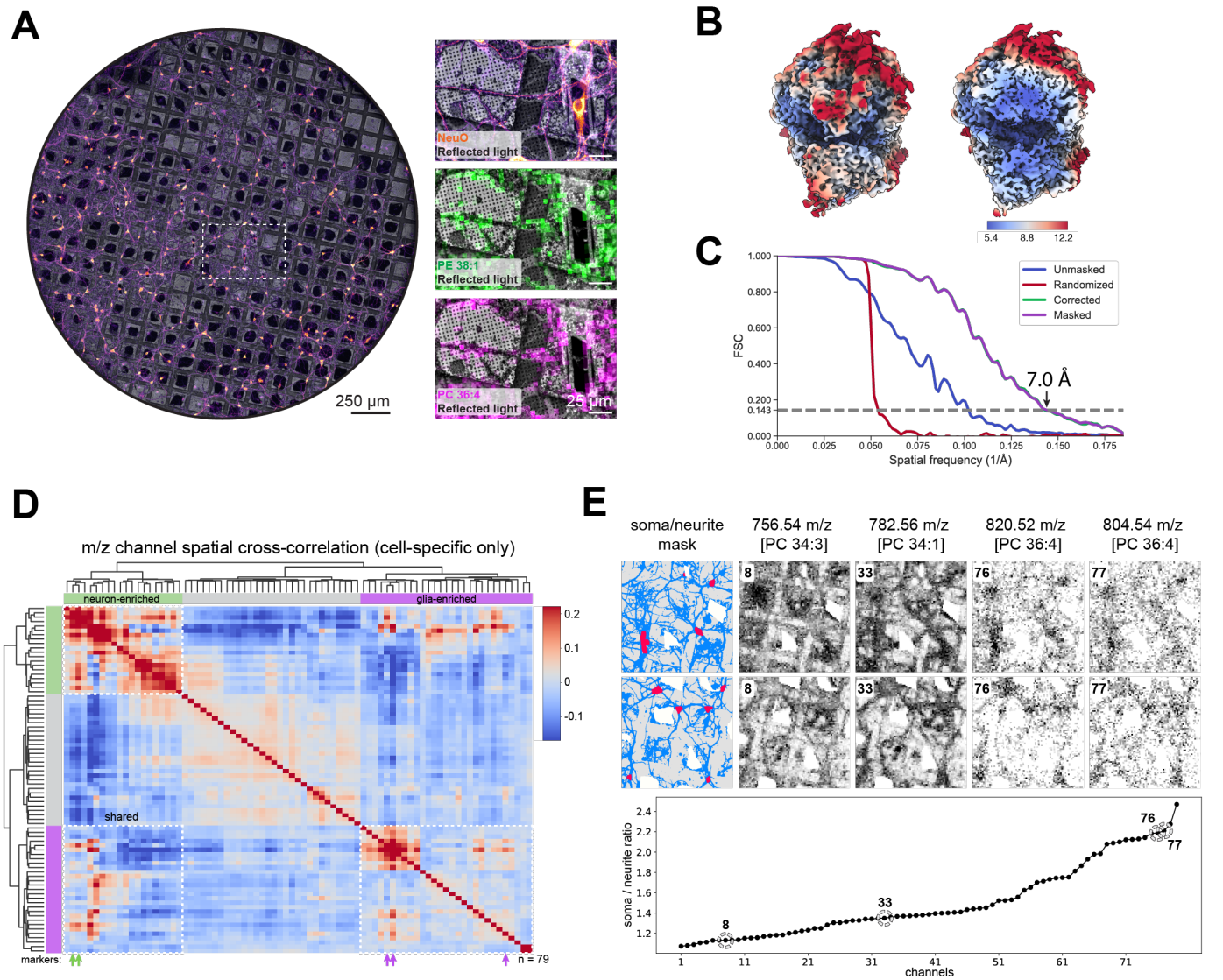

Figure 4: Mass spectrometry imaging of primary neuron culture grids. (A) Reflected light overview of primary neuron grid with correlated neuron-specific NeuO live-cell dye and cell-specific m/z channels. **(B)** Subtomogram average (STA) of 15,451 80S ribosomes, acquired from the grid in (A), color-coded by local resolution. This represents a subset of a previously published larger dataset. **(C)** Fourier shell correlation plot of STA in (B) with global resolution of 7.0 Å at 0.143 criterion. **(D)** Hierarchical clustering of cell specific m/z channels from primary neuron grid in (A) (n=79) shows three prominent clusters. Marker channels specific for neurons (green arrows) or glia cells (magenta arrows) identified in (Asadian et al, 2025) identify the clusters as neuron-enriched and glia-enriched m/z channels respectively. Lots of channels show elevated cross-correlation between them however ("shared"). **(E)** m/z intensity ratios between neuron soma and neurite masks. Individual m/z channels with high or low soma/neurite ratio are highlighted and representative images are displayed alongside the mask used for quantification. Blue = neurites, red = somata.

Interactive data integration in *SpatialData*

Finally, in order to enable streamlined analysis of correlated reflected and fluorescence light, cryo-ET and MSI data, we set out to integrate the different imaging modalities in a single software environment. Making use of the *SpatialData* framework (Marconato et al, 2025) **(Figure 5A-B)**, we provide an integrated pipeline for registration of all imaging modalities, as well as conversion scripts and notebooks to stitch, visualize and analyze them seamlessly. Besides raw data modalities, derived data such as masks, reconstructed tomograms, segmentations and particle coordinates including macromolecular activity states can also be integrated and queried without additional effort **(Figure 5B-C)**. For cellular identification and classification, fluorescence and MS Imaging data can thus be directly correlated to individual lamellae, enabling fast, comprehensive and informed analyses of that cell's molecular contents and ultrastructure.

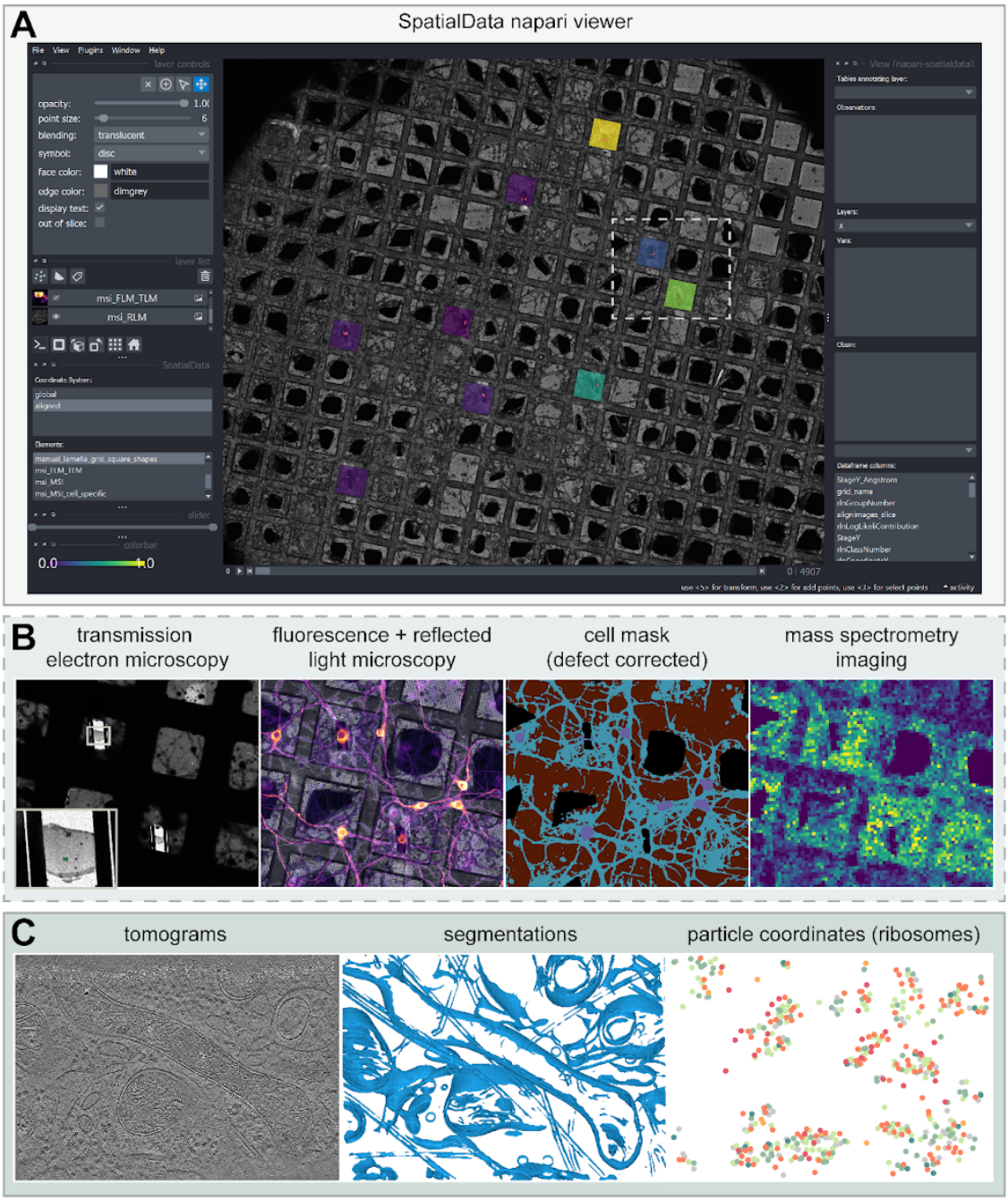

Figure 5: Multimodal integration of MSI and optical microscopy data in *SpatialData*. (A) *SpatialData* napari viewer interface with loaded primary neuron grid reflected light image and lamella grid square shapes. Grid square shapes are color-coded by percentage of all active ribosomes (viridis) within each lamella as determined by subtomogram averaging and classification. Values are attached to each lamella shape in the *SpatialData* object. **(B)** Enlarged views of area highlighted in (A) for integrated transmission electron microscopy, reflected and fluorescence light microscopy, cell masks, and a single mass spectrometry imaging m/z channel. **(C)** Enlarged views of lamella area highlighted in (B, left panel inset) showing integrated tomogram, corresponding membrane segmentation, and particle coordinates for identified ribosomes as points. Ribosome points are color-coded by translation state from active (greens) to inactive (reds)

Discussion

Here we present a novel, integrated pipeline combining MS Imaging and *in situ* cryo-ET. We developed a workflow that enables MALDI-MS-Imaging data acquisition directly from EM grids that were previously analyzed using FIB-milling and cryo-ET. The acquired data allow unambiguous identification and analysis of single cells and differentiation of species as well as cell types.

This was enabled by the design and construction of a custom-built holder for clipped cryo-EM grids, and the implementation of a gentle freeze-drying workflow directly within the microscope column. We first applied our pipeline to HeLa cells to show that we can achieve sufficient resolution and sensitivity to detect individual cells, and assess the intercellular variability in lipidome composition. All of this is enabled by the unbiased and holistic analysis of m/z peaks or channels via spatial cross-correlation and hierarchical clus-

tering to identify cell-specific and condition-specific channels. Our single-cell HeLa data match the results of other groups studying HeLa cells using MSI, with similar lipidome compositions and intercellular heterogeneity (Schober et al., 2012; Xi et al., 2020; Otsuka et al., 2025). Examining FIB-milled sections, we observed clear signals for cell bodies with the signature m/z channels of uncut cells. A certain degree of radiation damage was visible directly adjacent to the FIB-milled sections, but did not interfere with cell assignment. We next conducted a species-mixing experiment to show that we can differentiate between HeLa and *Polytomella* cells - two distantly related species. Using unsupervised clustering, we found that the MSI data segregates clearly into two groups allowing unambiguous assignment of the two species. To confirm our lipid assignments, we conducted two validation experiments: We first acquired independent LC-MS/MS-based lipidomics data of HeLa and *Polytomella* cells to generate a lipid reference library. Then we performed on-grid MALDI-MS/MS measurements of selected candidates to confirm the identity of these specific lipid species. We then challenged our MSI data-based cell species assignments for FIB-milled cells using the tomograms reconstructed from these lamellae, making use of the characteristic shape of the cristae in *Polytomella* and HeLa mitochondria. HeLa and *Polytomella* cells were assigned identically, confirming MSI-based classification. Next we examined if we could apply our workflow to primary neurons, which contain multiple cell types and grow much more densely. Unsupervised clustering of the MSI data allowed clear assignment of glia cells and neurons, making use of previously published data on cell type-specific lipids (Asadian et al., 2025) as marker channels. We also found that certain phospholipids were more abundant in the soma compared to neuronal processes, highlighting the potential of the technique to address study subcellular lipidome composition and dynamics.

From a technical point of view, there were two main challenges to overcome: Gentle drying of the ice-embedded cryo-ET samples and direct loading of the cryo-ET grid into the mass spectrometer. Freeze-drying directly in the stage of the electron microscope proved to be a gentle and direct way to preserve cellular structures without damaging the grid. Other drying approaches lead to cells rupturing on the grids, inducing a loss of spatial information and signal intensity. Notably, in this workflow, we retain all components of the medium the cells were grown in, as no additional washing steps are conducted. Initial attempts of the full drying process in the cryo-stage took around 24 h but were later routinely carried out remotely overnight. Even though this step does not require any manual handling in the cryo-stage of the EM, it is the most time-consuming part of the workflow and could be optimized in the future.

For grid transfer, we designed a holder that fits directly into standard MALDI adapters and can also be used for sublimation for matrix application (design files available upon request). The embedded magnet-held flat springs used to fix the clipped rings into the holder were essential, as pressure changes in the instrument could otherwise push the EM grids off the holder and into the instrument. We also added teaching marks and reference points on the holders for convenience and basic image alignment. High-resolution co-registration is relatively simple for the EM grids, as the repetitive background pattern (grids bars) provides an excellent network of evenly spaced and clearly recognizable reference points for alignment.

Our approach addresses one of the key challenges for *in situ* cryo-ET: establishing or confirming the identity of FIB-milled cells, and differentiating cell type and possibly even their metabolic states. At present, cellular identity and state can typically be determined using three main approaches: 1) correlative imaging via expression of fluorescent (or otherwise recognizable) proteins in the target cells or application of specific dyes (Pierson et al, 2024; Fung et al, 2023), including fluorescent indicators (Jung et al, 2025); and 2) subtomogram averaging of corresponding macromolecules that inform about the cell identity or state (e.g. ribosomes) (Rodrigues-Oliveira et al, 2023) Fluorescent imaging and the use of specific dyes offer high confidence cell identification prior to target selection, but require either genetic modification of the target cells or rely on the availability of such dyes. They also might lead to changes in the target cell's metabolism and structure. In addition, targeted detection of a single reporter protein may not capture the full heterogeneity of a sample. The use of subtomogram averaging and classification of relevant macromolecules on the other hand allow insights on cell identity or state from the same dataset without further modification, but are both time consuming and require extensive knowledge of the target biology. They also rely on the fact that macromolecules can be identified, averaged, and are sufficiently informative or distinct. Compared to these other approaches, MS Imaging combines the advantages of not requiring any sample modifications prior to analysis, fast data acquisition in less than 36 h for the entire workflow for a full EM grid at 5 μm pixel size (<24 h freeze-drying, 2 h sample processing, 10 h data acquisition) and detailed data of the cellular lipidome. In addition, our workflow is extremely robust and can be applied even to "old" cryo-ET samples: some of the grids we analyzed were stored for up to 12 months in liquid nitrogen after FIB-milling and cryo-ET data acquisition, and after freeze-drying for several weeks at 4°C.

Taken together, MS Imaging can be used post-hoc on any cryo-ET samples that were kept after EM data acquisition. So while MS Imaging data are not as comprehensive as transcriptomics, cellular species and subtypes can thus be unambiguously assigned in a fraction of the time needed for a full sequencing experiment. In addition, derivatisation approaches to increase detectability of specific analytes such as neurotransmitters (Shariagatorji et al., 2019) could expand the scope of such analyses significantly.

One clear limitation of MS Imaging at present, however, comprises its rather limited spatial resolution. Our pixel size of 5 μm comprises state-of-the-art MSI resolution, which is

sufficient for most eukaryotic cells but not capable of distinguishing most prokaryotic cells. Other custom and developmental MALDI setups offer sub-2-µm pixel size (Young et al., biorxiv 2025, Kompauer et al., 2016), but employ a transmission-based laser setup which is not usable for our current version of the grid holder or have a relatively slow laser that would make scanning a full grid very time-consuming. Further development of these setups could, however, significantly improve resolution and sensitivity for on-grid MSI. Realistically, though, sub-micrometer resolution would be needed to discern subcellular features and organelles within the soma, or directly analyze lamellae post cryo-ET analysis. SIMS-MS Imaging based approaches offer this resolution already, but with very few exceptions are limited to inorganic molecules and metals (Tian et al., 2024; Costa et al., 2025; Uzoni et al., 2025). We anticipate that this technology, possibly in instruments combining SIMS-MS and EM, could allow direct classification and selection of cells on grids for FIB-milling and cryo-ET analysis in the future.

Going forward, we suggest to consider post cryo-ET analyses during the FIB-milling process. The lamellae analyzed in this study were mostly prepared before our implementation of this workflow and thus cut to maximize the cross-section of the cell bodies, not to maximize MSI acquisition area. In fact, in some cases the lamellae were cut in such a way that almost the complete cell was ablated and only a fraction of the density remained. In such a scenario, MS Imaging and any other post-cryo-ET method often do not provide sufficient signal intensities for unambiguous cell identification. Going forward, FIB-milling could be conducted in such a way that a larger section of the cell the lamella is cut from is left intact, to provide an abundant source of signal for unambiguous identification *post hoc*.

In an effort to help bridge the structural and molecular data ecosystems, we developed and deposited a set of alignment and data conversion routines and examples for the multi-omics python framework *SpatialData* (Marconato et al, 2025). This enables full integration of various modalities including optical, fluorescence and MS imaging, as well as raw and derived cryo-ET data such as grid and lamella images, tomograms, segmentations, particle positions and functional states - all in the same multi-scale coordinate system. The fully co-registered data can be directly examined in all imaging modalities within a napari viewer, enabling comprehensive evaluation and interpretation of the data. At present, comprehensive MS Imaging and lipidomics data are already available for many well-studied model systems, offering a robust starting point for cellular characterization in such a combinatorial approach. Going forward, with more single-cell lipidomics MSI data becoming available, we anticipate that cellular classification could be conducted as routinely as clinical "Biotyping", where pathogens are identified based on empirical MALDI-MS data (Mellmann et al., 2008). Full integration of these pipelines in the same software environment would facilitate direct species classification and possibly also enable analyses of their functional states. We believe that this approach could be particularly useful for environmental samples, in which multiple different organisms could be present. In this scenario, MALDI-MS Imaging can provide robust, sensitive and comprehensive data for cell species assignment.

Conclusion

Taken together, here we present the first fully integrated pipeline using MS Imaging for the identification and classification of cells that were analyzed using cryo-ET. Our workflow offers fast and reliable identification of cell species and type, does not require any biochemical or genetic modification of the sample or host organism, and can be used on any cryo-ET sample submitted to FIB-milling. We anticipate that integration of MS Imaging will provide complementary and essential information for *in situ* cryo-ET, in particular for studying heterogeneous samples containing multiple species or distinct functional states in mixed cell populations. To fully exploit such an integrative workflow, future development will focus on improving MSI spatial resolution to sub-micrometer pixel size as well as different derivatisation strategies to expand MSI detection to e.g. metabolic marker molecules or neurotransmitters. Then this integrated approach could change the way that structural biologists think about and conduct *in situ* cryo-ET, as sample heterogeneity and cellular identity can be resolved quickly and robustly, with detailed information on cell species and type as well as its functional state.

References

Asadian, M., S. W. Croslow, T. J. Trinklein, S. S. Rubakhin, F. Lam and J. V. Asadian, M., S. W. Croslow, T. J. Trinklein, S. S. Rubakhin, F. Lam and J. V. Sweedler (2025). "High-Throughput Fluorescence-Guided Sequential Single-Cell MALDI-ICC Mass Spectrometry." Anal Chem **97**(29): 15864–15872.

Berg, S., D. Kutra, T. Kroeger, C. N. Straehle, B. X. Kausler, C. Haubold, M. Schiegg, J. Ales, T. Beier, M. Rudy, K. Eren, J. I. Cervantes, B. Xu, F. Beuttenmueller, A. Wolny, C. Zhang, U. Koethe, F. A. Hamprecht and A. Kreshuk (2019). "ilastik: interactive machine learning for (bio)image analysis." Nature Methods **16**(12): 1226–1232.

Bien, T., K. Koerfer, J. Schwenzfeier, K. Dreisewerd and J. Soltwisch (2022). "Mass spectrometry imaging to explore molecular heterogeneity in cell culture." Proceedings of the National Academy of Sciences **119**(29): e2114365119.

Costa, C., J. v. Gerichten, V. Palitsin, G. W. Grime, S. J. Hinder, N. Sano, R. Webb and M. J. Bailey (2025). "Multimodal Ion Beam Imaging to Correlate Elements and Metabolites at the Micron Scale Using Water Cluster Secondary Ion Mass Spectrometry and MeV Ion Beam Analysis." Analytical Chemistry **97**(30): 16573–16582.

Costa, C., J. v. Gerichten, V. Palitsin, G. W. Grime, S. J. Hinder, N. Sano, R. Webb and M. J. Bailey (2025). "Multimodal Ion Beam Imaging to Correlate Elements and Metabolites at the Micron Scale Using Water Cluster Secondary Ion Mass Spectrometry and MeV Ion Beam Analysis." Analytical Chemistry **97**(30): 16573–16582.

de Chaumont, F., S. Dallongeville, N. Chenouard, N. Hervé, S. Pop, T. Provoost, V. Meas-Yedid, P. Pankajakshan, T. Lecomte, Y. Le Montagner, T. Lagache, A. Dufour and J.-C. Olivo-Marin (2012). "Icy: an open bioimage informatics platform for extended reproducible research." Nature Methods **9**(7): 690–696.

Dietrich, L., A.-N. A. Agip, C. Kunz, A. Schwarz and W. Kühlbrandt (2024). "In situ structure and rotary states of mitochondrial ATP synthase in whole Polytomella cells." Science **385**(6713): 1086–1090.

Dietrich, L., A.-N. A. Agip, C. Kunz, A. Schwarz and W. Kühlbrandt (2024). "In situ structure and rotary states of mitochondrial ATP synthase in whole Polytomella cells." Science **385**(6713): 1086–1090.

Fung, H. K. H., Y. Hayashi, V. T. Salo, A. Babenko, I. Zagoriy, A. Brunner, J. Ellenberg, C. W. Müller, S. Cuylen-Haering and J. Mahamid (2023). "Genetically encoded multimeric tags for subcellular protein localization in cryo-EM." Nature Methods **20**(12): 1900–1908.

Hagen, W. J. H., W. Wan and J. A. G. Briggs (2017). "Implementation of a cryo-electron tomography tilt-scheme optimized for high resolution subtomogram averaging." Journal of Structural Biology **197**(2): 191–198.

Jung, M., G. Ko, D. Lim, S. Kim, S. Kim, Y.-J. Kim, M. Choi and S.-H. Roh (2025). "CoVET: Cryo-Electron Tomography guided by optical electrophysiology." bioRxiv: 2025.2005.2014.653951.

Kompauer, M., S. Heiles and B. Spengler (2017). "Atmospheric pressure MALDI mass spectrometry imaging of tissues and cells at 1.4-µm lateral resolution." Nature Methods **14**(1): 90–96.

Lamm, L., R. D. Righetto, W. Wietrzynski, M. Pöge, A. Martinez-Sanchez, T. Peng and B. D. Engel (2022). "MemBrain: A deep learning-aided pipeline for detection of membrane proteins in Cryo-electron tomograms." Computer Methods and Programs in Biomedicine ***224***: 106990.

Mahamid, J., S. Pfeffer, M. Schaffer, E. Villa, R. Danev, L. Kuhn Cuellar, F. Förster, A. A. Hyman, J. M. Plitzko and W. Baumeister (2016). "Visualizing the molecular sociology at the HeLa cell nuclear periphery." Science **351**(6276): 969–972.

Marconato, L., G. Palla, K. A. Yamauchi, I. Virshup, E. Heidari, T. Treis, W.-M. Vierdag, M. Toth, S. Stockhaus, R. B. Shrestha, B. Rombaut, L. Pollaris, L. Lehner, H. Vöhringer, I. Kats, Y. Saeys, S. K. Saka, W. Huber, M. Gerstung, J. Moore, F. J. Theis and O. Stegle (2025). "SpatialData: an open and universal data framework for spatial omics." Nature Methods **22**(1): 58–62.

Mastronarde, D. N. (2003). "SerialEM: A Program for Automated Tilt Series Acquisition on Tecnai Microscopes Using Prediction of Specimen Position." Microscopy and Microanalysis **9**(S02): 1182–1183.

Medina, M., Y.-T. Chang, H. Rahmani, D. Fuentes, B. A. Barad and D. A. Grotjahn (2025). "Surface morphometrics reveals local membrane thickness variation in organellar subcompartments." bioRxiv: 2025.2004.2030.651574.

Mellmann, A., J. Cloud, T. Maier, U. Keckevoet, I. Ramminger, P. Iwen, J. Dunn, G. Hall, D. Wilson, P. Lasala, M. Kostrzewa and D. Harmsen (2008). "Evaluation of matrix-assisted laser desorption ionization-time-of-flight mass spectrometry in comparison to 16S rRNA gene sequencing for species identification of nonfermenting bacteria." J Clin Microbiol **46**(6): 1946–1954.

Nguyen, H. T. D., G. Perone, N. Klena, R. Vazzana, F. Kaluthantrige Don, M. Silva, S. Sorrentino, P. Swuec, F. Leroux, N. Kalebic, F. Coscia and P. S. Erdmann (2024). "Serialized on-grid lift-in sectioning for tomography (SOLIST) enables a biopsy at the nanoscale." Nature Methods **21**(9): 1693–1701.

Ochner, H., B. Isbilir, S. Blasche, D. Scheidweiler, Y. Zhang, Z. Wang, T. Smith, C. Franco, R. Bradley, K. R. Patil and T. A. M. Bharat (2025). "Sub-cellular chemical mapping in bacteria using correlated cryogenic electron and mass spectrometry imaging." bioRxiv: 2025.2008.2029.673036.

Otsuka, Y., K. Kabayama, A. Miura, M. Takahashi, K. Hata, Y. Izumi, T. Bamba, K. Fukase and M. Toyoda (2025). "Single-cell mass spectrometry imaging of lipids in HeLa cells via tapping-mode scanning probe electrospray ionization." Communications Chemistry **8**(1): 147.

Paul-Gilloteaux, P., X. Heiligenstein, M. Belle, M.-C. Domart, B. Larijani, L. Collinson, G. Raposo and J. Salamero (2017). "eC-CLEM: flexible multidimensional registration software for correlative microscopies." Nature Methods **14**(2): 102–103.

Pettersen, E. F., T. D. Goddard, C. C. Huang, E. C. Meng, G. S. Couch, T. I. Croll, J. H. Morris and T. E. Ferrin (2021). "UCSF ChimeraX: Structure visualization for researchers, educators, and developers." Protein Sci **30**(1): 70–82.

Pierson, J. A., J. E. Yang and E. R. Wright (2024). "Recent advances in correlative cryo-light and electron microscopy." Current Opinion in Structural Biology **89**: 102934.

Rappez, L., M. Stadler, S. Triana, R. M. Gathungu, K. Ovchinnikova, P. Phapale, M. Heikenwalder and T. Alexandrov (2021). "SpaceM reveals metabolic states of single cells." Nat Methods **18**(7): 799–805.

Rodrigues-Oliveira, T., F. Wollweber, R. I. Ponce-Toledo, J. Xu, S. K. M. R. Rittmann, A. Klingl, M. Pilhofer and C. Schleper (2023). "Actin cytoskeleton and complex cell architecture in an Asgard archaeon." Nature **613**(7943): 332–339.

Schaffer, M., S. Pfeffer, J. Mahamid, S. Kleindiek, T. Laugks, S. Albert, B. D. Engel, A. Rummel, A. J. Smith, W. Baumeister and J. M. Plitzko (2019). "A cryo-FIB lift-out technique enables molecular-resolution cryo-ET within native Caenorhabditis elegans tissue." Nature Methods **16**(8): 757–762.

Schindelin, J., I. Arganda-Carreras, E. Frise, V. Kaynig, M. Longair, T. Pietzsch, S. Preibisch, C. Rueden, S. Saalfeld, B. Schmid, J.-Y. Tinevez, D. J. White, V. Hartenstein, K. Eliceiri, P. Tomancak and A. Cardona (2012). "Fiji: an open-source platform for biological-image analysis." Nature Methods **9**(7): 676–682.

Schiøtz, O. H., C. J. O. Kaiser, S. Klumpe, D. R. Morado, M. Poege, J. Schneider, F. Beck, D. P. Klebl, C. Thompson and J. M. Plitzko (2024). "Serial Lift-Out: sampling the molecular anatomy of whole organisms." Nature Methods **21**(9): 1684–1692.

Schober, Y., S. Guenther, B. Spengler and A. Römpp (2012). "Single cell matrix-assisted laser desorption/ionization mass spectrometry imaging." Anal Chem **84**(15): 6293–6297.

Shariatgorji, M., A. Nilsson, E. Fridjonsdottir, T. Vallianatou, P. Källback, L. Katan, J. Sävmarker, I. Mantas, X. Zhang, E. Bezard, P. Svenningsson, L. R. Odell and P. E. Andrén (2019). "Comprehensive mapping of neurotransmitter networks by MALDI-MS imaging." Nat Methods **16**(10): 1021–1028.

Tegunov, D., L. Xue, C. Dienemann, P. Cramer and J. Mahamid (2021). "Multi-particle cryo-EM refinement with M visualizes ribosome-antibiotic complex at 3.5 Å in cells." Nature Methods **18**(2): 186–193.

Tian, H., P. Rajbhandari, J. Tarolli, A. M. Decker, T. V. Neelakantan, T. Angerer, F. Zandkarimi, H. Remotti, G. Frache, N. Winograd and B. R. Stockwell (2024). "Multimodal mass spectrometry imaging identifies cell-type-specific metabolic and lipidomic variation in the mammalian liver." Developmental Cell **59**(7): 869–881.e866.

Uzoni, S., D. Zanchin, V. Chatzikyriakos, N. Neittaanmäki and J. S. Fletcher (2025). "Mapping the Molecular Landscape of Human DLBCL by GCIB-SIMS." Analytical Chemistry **97**(13): 7186–7194.

Wang, Z., M. Grange, T. Wagner, A. L. Kho, M. Gautel and S. Raunser (2021). "The molecular basis for sarcomere organization in vertebrate skeletal muscle." Cell **184**(8): 2135–2150.e2113.

Xi, Y., A. Tu and D. C. Muddiman (2020). "Lipidomic profiling of single mammalian cells by infrared matrix-assisted laser desorption electrospray ionization (IR-MALDESI)." Analytical and Bioanalytical Chemistry **412**(29): 8211–8222.

Young, R. S. E., A.-K. Piper, L. McAlary, J. C. McKinnon, J. S. Lum, J. Soltwisch, M. Niehaus and S. R. Ellis (2025). "Subcellular mass spectrometry imaging of lipids and nucleotides using transmission geometry ambient laser desorption and plasma ionisation." bioRxiv: 2025.2005.2013.653655.

Zheng, S., G. Wolff, G. Greenan, Z. Chen, F. G. A. Faas, M. Bárcena, A. J. Koster, Y. Cheng and D. A. Agard (2022). "AreTomo: An integrated software package for automated marker-free, motion-corrected cryo-electron tomographic alignment and reconstruction." J Struct Biol X **6**: 100068.

Zivanov, J., T. Nakane, B. O. Forsberg, D. Kimanius, W. J. H. Hagen, E. Lindahl and S. H. W. Scheres (2018). "New tools for automated high-resolution cryo-EM structure determination in RELION-3." eLife **7**: e42166.

Acknowledgements

We would like to thank the MPI for biophysics, in particular Dr. Martin Beck and Dr. Werner Kühlbrandt for allowing us to access their cryo-EM infrastructure and the Frankfurt Central Electron Microscopy facility, in

particular Dr. Sonja Welsch and Dr. Maarten Tujtel for training and continued support, as well as detailed discussions on the freeze-drying process. For excellent technical assistance, we would like to thank Imke Wüllenweber (lipidomics sample preparation), Fabian Baur (grid holder production) and Steffen Rebenich (laser milling).

A.S. acknowledges funding by EMBO (postdoctoral fellowship, ALT 836-2020) and the Peter und Traudl Engelhorn Stiftung.

This paper was typeset with the bioRxiv word template by @Chrelli: www.github.com/chrelli/bioRxiv-word-template

Competing interest statement

A.B. is an employee of Bruker Daltonics, the company that manufactures the mass spectrometer used in this study.

Materials and Methods

Cell culturing and grid preparation

HeLa cells

EM grids (Quantifoil Au200 R2/2) were coated with fibronectin from human plasma (0.01%) overnight. Subsequently, grids were washed with ddH_2O and stored in ddH_2O until use. For cell seeding, each chamber of a Millicell EZ 8-well slide was filled with 40 µl DMEM (high glucose) medium (Gibco) before transferring one grid each into each well. Cells were seeded by adding 40 µl of cell suspension to each grid (final cell count: 40,000 cells/grid). Cells were incubated overnight at 37°C, 5% CO_2. After 24 h, grids were blotted for 4 s and plunge frozen in liquid ethane using a Leica GP2 plunge freezer.

Polytomella

Polytomella cells were cultured as described previously (Dietrich et al, 2024). In short, 50 ml MAP media was inoculated with 10 µl of *Polytomella* cell culture and grown at room temperature without agitation for 48 h until OD_{600} = 0.9. For grid preparation, 3 µl culture was applied to EM grids (Quantifoil Cu200 R2/2) prior to blotting (3.5 s) and plunge freezing in liquid ethane using the Leica GP2 plunge freezer.

HeLa & Polytomella species mixing experiment

HeLa cells were seeded as described above. In addition, prior to freezing, 3 µl of *Polytomella* cell culture (OD_{600} = 0.9) were applied to the grid, blotted for 4 s and plunge frozen using a Leica GP2 plunge freezer.

Rat hippocampal primary brain cells

The grids containing primary rat hippocampal brain cells had previously been grown, acquired, and remained in liquid nitrogen storage [ref]. In this work, we used one of these grids. Briefly, rat hippocampal neurons were prepared from P0-P1 rat pups (Sprague Dawley, IGS, Crl:CD(SD), Charles River Laboratories). The hippocampus was dissected, digested with Papain (Sigma), and plated at 140,000 cells/ml on glass bottom dishes (P35G-1.5-14-C, Mattek) containing one EM grid each (Quantifoil Au200 R2/2), coated with 0.1 mg/ml poly-D-lysine (BD). After 4 h, 700 µl glia-conditioned medium was added and cells were cultured for 21 days at 37 °C in 5% CO2 with the addition of 700 µl normal growth media (NGM; Neurobasal A (Invitrogen/Gibco) without phenol red, supplemented with B27 (Invitrogen/Gibco) and GlutaMAX (Gibco)) every week. Neurons were imaged in medium supplemented with NeuO (0.25 µM, Stemcell Technologies) and 20 mM HEPES and plunge frozen in liquid ethane, on a Leica GP2 plunge freezer with 10 s blotting time.

Cryo-FIB milling

Cryo-FIB milling was performed using a ThermoFisher Aquilos 2 dual beam microscope. Grids were coated with organometallic platinum for 13 s using the gas injection system (GIS) and sputter coated with inorganic platinum for 20 s. At this point, the previously acquired NeuO images were imported and correlated in 2D using the MAPS software. FIB sample thinning was conducted manually at a milling angle of 11° in several steps: First, vertical micro-expansion joints were cut at 1 nA current, followed by horizontal cuts spaced 5 µm apart at 1 nA, 3 µm at 0.5 nA, 1 µm at 0.3 nA, and finally lamella polishing at 180 - 230 nm distance and 30 pA current. A final sputter coating of inorganic platinum for 1-2 s was performed and grids were stored in liquid nitrogen until TEM acquisition. For mixed HeLa / *Polytomella* grids, lamellae were prepared automatically using the AutoTEM software.

Cryo electron tomography

For primary hippocampal neuron grids, TEM grid/lamella overviews as well as tilt series were previously acquired (Manuscript submitted). Briefly, all data used in this study was acquired on a Titan Krios G2 transmission electron microscope (Thermo Scientific), operated at 300 keV in EFTEM mode via SerialEM (Mastronarde, 2003) equipped with a BioQuantum K3 imaging filter (Gatan). In order to first identify suitable lamellae regions and then suitable subcellular regions, lower magnification montage images were acquired at 135x / 6,500x nominal magnification and 0 / -50 µm defocus respectively. Suitable positions for tilt series acquisition were then acquired using the tilt controller via the dose symmetric tilt scheme (Hagen et al, 2017) from -49° to +63° (with +11° pre-tilt) and -60° to +60° (no pre-tilt) for neurites in 2° increments with a pixel size of 2.682 Å/px (33,000x nominal magnification) and an energy filter slit width of 20 eV. A total dose of ~120 e-/Å2 was distributed over the corresponding 58 and 61 tilts, amounting to ~2.2 and ~1.9 e-/Å2/tilt respectively and divided into 10 frames with on-the-fly motion correction in SerialEM. Successive tilt series were acquired in batch at -2.5 to -4.5 µm defocus with -0.25 µm increment. Settings were identical for all datasets.

Subtomogram averaging of neuronal ribosomes

The full dataset containing ~284,000 ribosomes was previously processed to a global resolution of the consensus map of 5.4 Å (manuscript submitted). For this work, this dataset was subset to only entail ribosomes originating from the single grid depicted in Fig. 4A. This yielded 15,451 particles. A particle list containing these was subjected to automatic 3D refinement in region (v3.1) (Zivanov et al., 2018), followed by a single round of refinement in M (Tegunov et al., 2021). Translation state designations depicted in Fig. 5 were adapted from the classification of the full dataset.

HeLa/*Polytomella* tomogram reconstruction and membrane segmentation

Acquired tilt series for mixed HeLa/*Polytomella* grids were reconstructed using AreTomo2 (Zheng et al., 2022) using `AreTomo2 -InMrc ../${tomoNumber}.mrc -OutMrc ${tomoNumber}.mrc -LogFile 1 -AngFile ${tomoNumber}.rawtlt -VolZ 2000 -PixSize 2.682 -Kv 300 -Cs 2.7 -TiltCor 0 -OutBin 6 -Wbp 1 -DarkTol 0.7 -OutImod 2 -FlipVol 1` and membranes were automatically segmented using membrain-seg (v1, model 10α) (Lamm et al., 2022). The resulting segmentations were cleaned and selected for mitochondrial membranes in ChimeraX (v1.9) (Pettersen et al., 2021) using `erase sphere` and `hide dust`.

Freeze-drying and storage

For freeze-drying, cryo-EM grids were loaded (back) into the ThermoFisher Aquilos 2 dual beam microscope. At a constant pressure of ~2-4 $\times 10^{-7}$ mbar, the stage temperature was gradually raised to ~-90^{0}C - -85^{0}C by adjusting the nitrogen flow rate. This target temperature was chosen to maximize sublimation rate while minimizing recrystallization, but depending on the application, a higher temperature and thus faster drying processes might be preferable. The exact flow rate necessary depends on the microscope setup and will have to be determined empirically. Slight changes to hardware configuration have led to significant changes in target flow rate on our setup before. Cells and lamellae were monitored before and during the drying process via a built-in widefield fluorescence microscope in reflected light mode and judged by a change in the interference patterns over time. No imaging via SEM or FIB beams was performed once the temperature was raised to avoid radiation damage. Drying generally occurred in two phases: First the surrounding medium disappeared, followed by specimen shrinkage. Once no more changes were observed (typically on the order of 4 hours), the microscope was brought to room temperature by reducing the flow to 0, typically overnight. Grids were then removed from the microscope and stored in a desiccated environment at 4^{0}C until further use. We typically use a 50 ml plastic tube with silica beads in a refrigerator.

MSI autogrid holder design & fabrication

The Autogrid holder was designed to securely fix EM grids during matrix applications and imaging measurements. It is compatible with standard target frames for specimen carriers and features precisely milled grooves that ensurestable x/y-positioning of the grids while compensating for the sample height caused by clamping rings. Fixation in the z-direction is achieved by

flat springs attached to magnets integrated into the adapter base. The design was created using the CAD software *Solidworks 2022* (Dassault Systèmes). The base holder was manufactured on a 5-axis CNC machining center (HERMLE C 20 U, iTNC 530 Heidenhain control). The springs were produced using a laser processing center.

MSI matrix application by sublimation

Matrix application was performed with a custom-built sublimation apparatus. The EM-grids were mounted in the holder and the whole assembly attached to the cooling finger of the apparatus. Subsequently 25 mg DHB matrix were dissolved in acetone and distributed evenly in the pre-heated reservoir of the sublimation chamber matrix reservoir. After the evaporation of solvent the chamber was closed and the sublimation was carried out for 1.5 min at 170°C and a vacuum of 5*10^-2 mbar.

MSI data acquisition

MSI data were acquired on a timsTOF fleX MALDI-2 instrument (Bruker Daltonics) with microGrid mode turned on. Measurements were performed in positive mode with a mass range from 300-1700 m/z and TIMS enabled with a mobility range from 0.7-1.95 V*s/cm^2. Mass calibration was performed with red phosphorus clusters on the target and ion mobility was calibrated with Tunemix. All imaging experiments were acquired with a raster size of 5*5µm and 30 laser shots/pixel.

MSI data processing and compound annotation

MSI data files were imported into Scils Lab and feature finding performed with the T-ReX3 algorithm using 10 ppm mass and 2 Å mobility interval widths, a 4x4 neighbourhood size, 100% spectra coverage and a minimum intensity of 50. All features were then exported as ome.tif image files for further spatial data analysis.
Compound annotations were obtained by matching exact masses and mobilities against target lists and rule-based annotations in Metaboscape 2024 and mzmine 4.7. Where possible lipid annotations were further validated with on-grid MS/MS experiments or LC-MS based lipidomics data from bulk cell extracts.

Data processing

Cross-correlation and clustering to identify cell-specific m/z channels

All identified peaks were exported as .ome.tif image files in the SCiLS Lab software without normalization and hotspot removal, and imported for analysis in python via the `tifffile` library. In order to identify channels with characteristic localizations to cells, grid bars, carbon film etc., we computed a cross-correlation matrix for all normalized channels (Fig. X, `numpy.corrcoef()`). This cross-correlation matrix was segmented via hierarchical clustering (`scipy.cluster.hierarchy.linkage()` and `scipy.cluster.hierarchy.fcluster()`). In order to identify clusters characteristic of cells, pre-selected marker channels encoding for several phosphatidyl choline species were used. All clusters containing such marker channels were then extracted and subjected to a second round of cross-correlation and clustering to identify homogeneous vs heterogeneous channels. All corresponding code including analysis notebooks can be found at:
https://gitlab.mpcdf.mpg.de/mpibr/spatialdata_et

Registration of imaging modalities

For precise registration of the various imaging modalities (fluorescence light microscopy, reflected light microscopy, transmission and scanning electron microscopy, mass spectrometry imaging), an identical set of landmark points was chosen for each image. The landmarks were placed in the same order and orientation for all modalities. If the full grid was visible the first point was chosen on the center grid intersection, which has a unique asymmetric shape for Quantifoil grids. Five points were then chosen going in each cardinal direction starting with the long, round side, followed by the short round side, the sharp edge and no edge. This order is arbitrary but has to be kept consistent between grids to account for potential flipping between imaging modalities. The landmark points were saved and imported into each software package used subsequently. For quantification, registration was then performed using the "Landmark correspondences" (https://github.com/axtimwalde/mpicbg/blob/master/mpicbg_/src/main/java/Transform_Roi.java) plugin in FIJI (Schindelin et al., 2012) as described below. For target registration error estimation it was performed using the ec-CLEM (Paul-Gilloteaux et al., 2017) plugin in icy (de Chaumont et al., 2012), and for visualization, the spatialdata (Marconato et al., 2025) library in python and napari (https://zenodo.org/records/16883660) was used, each as described below.

Creation of individual cell masks

Step by step illustrations for the entire workflow are available in Fig S2 exemplified for the HeLa grid displayed in Fig 2F. First, individual cells were manually segmented on the reflected light image using the "labels" function in napari (https://zenodo.org/records/16883660) and saved as a binary image. In parallel, a mask covering the acquired MSI area was produced via maximum intensity projection of all m/z channels followed by the "Fill holes" operation in FIJI. This binary mask was then registered and upsampled to the reflected light coordinate system using a set of landmark points described above using "Landmark correspondences" in FIJI. MSI landmark points were taken as source and RL landmark points as template, with "affine" transformation class, "least squares" and no interpolation. The resulting MSI area mask and the cell mask were then multiplied and individual cells were segmented using the watershed implementation in FIJI with manual curation.

Creation of soma / neurite masks

For the neuron grid displayed in Fig 4A, step by step illustrations for the entire workflow are available in Fig S4E. Individual cell somata and neurites were automatically segmented in the NeuO fluorescence microscopy image using the "Pixel classification" workflow in ilastik (Berg et al., 2019) using four labels: Cell somata, neurites, grid background, and empty regions. To account for defects during MSI preparation, a defect mask was produced from the reflected light image using "MinError(I)" thresholding in FIJI. This defect mask was registered to the cell mask as described above and multiplied to create a defect-corrected cell mask. Finally, to account for the MSI acquisition area, an MSI area mask was created as above via maximum intensity projection of all m/z channels followed by "Fill holes" in FIJI. This mask was also registered, transformed and upscaled into the fluorescence microscopy coordinate system and multiplied with the defect-corrected cell mask to produce the final mask used for quantification of m/z intensities in somata vs neurites described below.

Extracting MSI intensities for individual cell ROIs

In order to now extract intensity values for each ROI and each channel, the newly created mask alongside the reflected light and MSI image stacks were opened in FIJI. Registration points were manually chosen along the grid pattern in reflected light, transmission light or in grid bar specific m/z channels (Fig SX). Using a FIJI macro, for each channel, that channel was duplicated, registration positions were applied using the ROI manager and the channel was transformed to be registered with the mask using the "Landmark correspondences" plugin. MSI landmark points were taken as source and RL landmark points as template, with "affine" transformation class, "least squares" and no interpolation. For each ROI in the cell mask (which are now overlapping with the newly transformed MSI channel image), the mean MSI intensity values per area were then recorded using the "Measure" command in FIJI, concatenated and saved as csv file. Recorded mean m/z per area were next read and converted to a `pandas` DataFrame in python. Spectra for individual m/z channels were plotted as `matplotlib` bar plots for selected cells, and a principal component analysis was performed for all cells across all cell-specific channels and displayed as `matplotlib` scatter plot, color-coded by the intensity of channel 744.48 m/z.
For neuronal soma/neurite ratio measurements, the same macro was used but rather than recording a mean intensity value per cell ROI, a single value for the entire neurite mask area and the entire soma mask area was recorded. These were divided and plotted as `seaborn` line plot in python.

Target registration error estimation

In order to estimate the target registration error between MSI data and other registered modalities (such as reflected light), we used the ec-CLEM (Paul-Gilloteaux et al., 2017) plugin in icy (de Chaumont et al., 2012). For this we imported both images into ec-CLEM alongside the previously selected registration points (landmarks). The transformation was applied and the local target registration error for each pixel was calculated. The resulting heatmap was then cropped to contain only the source region of MSI data acquisition and displayed using viridis.

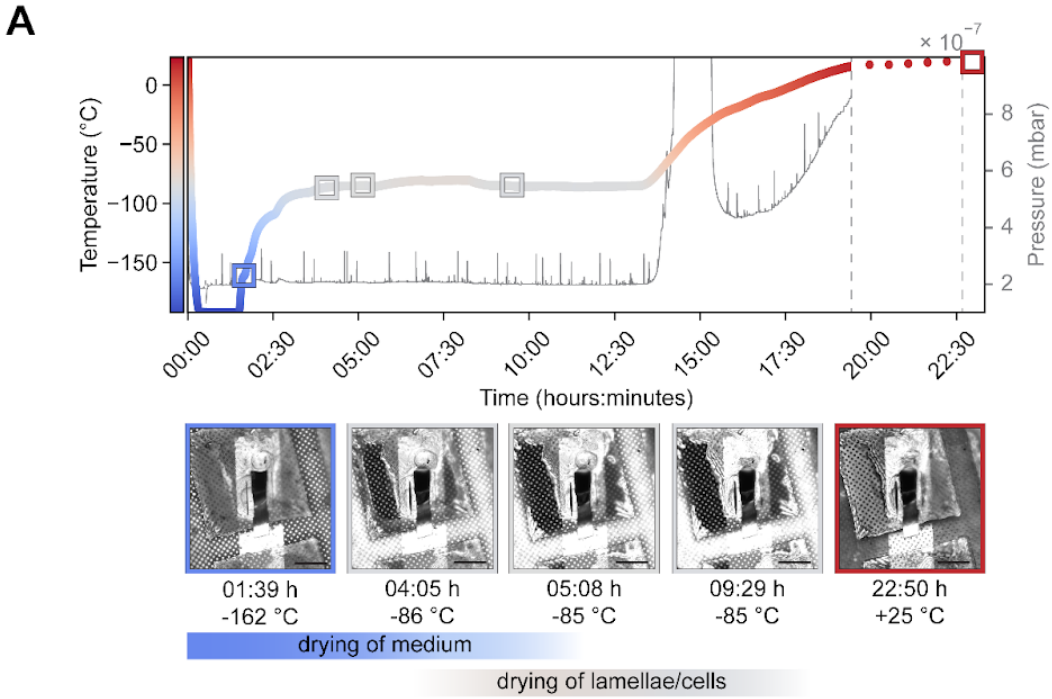

Figure S1: Freeze-drying progression and temperature profile. (A) Cryo-EM grids containing HeLa cells are freeze-dried within a FIB-SEM dual beam microscope chamber. Under constant chamber pressure (~2×10^{-7} mbar) grids are warmed to ~-85°C and monitored using reflected light imaging via a built-in widefield microscope. Individual snapshots are displayed showing the drying of residual cell culture medium, followed by drying of cells and lamellae as visible by interference patterns. When no further drying is observed, the stage is warmed to room temperature.

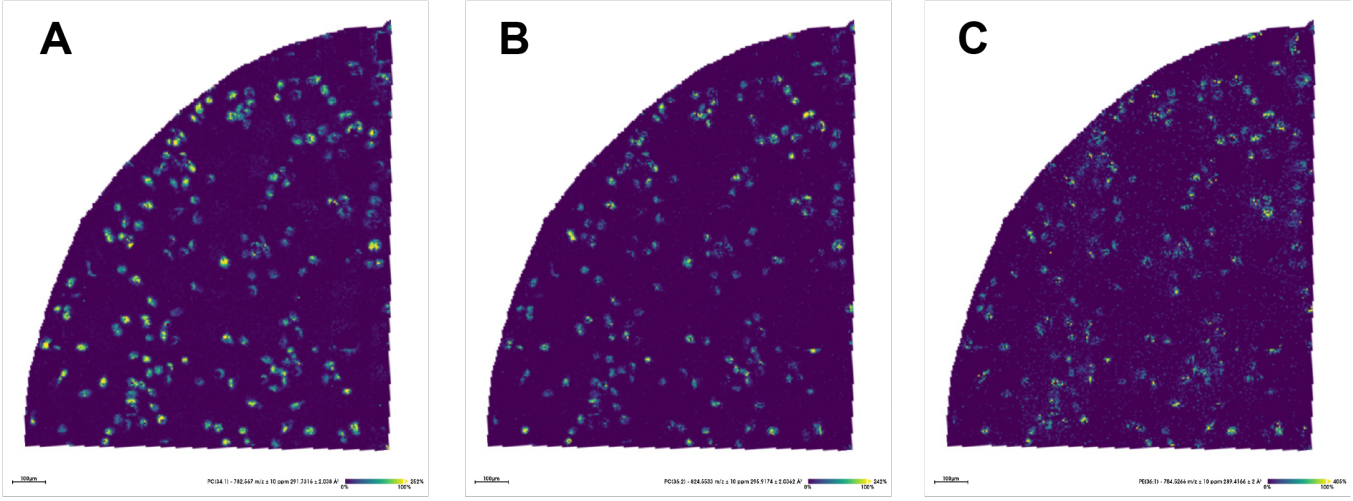

Figure S2: Examples for HeLa lipids. (A) PC 34:1, (B) PC 36:2, (C) PE 36:1.

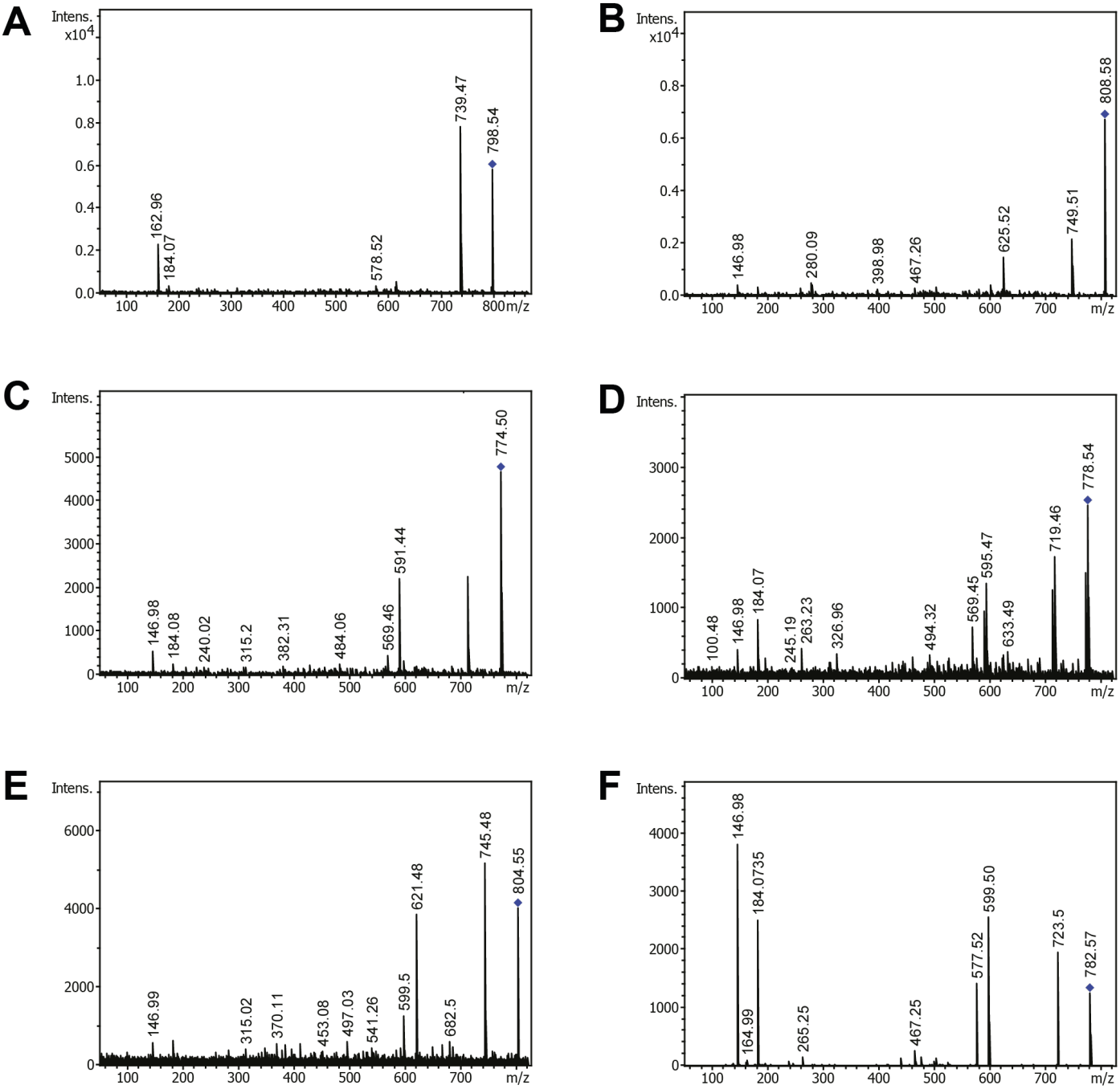

Figure S3: On-grid MS/MS spectra. (A) m/z 798.54 PC 34:1 (HeLa), (B) 808.58 PC 38:5 (HeLa), (C) 774.5 PC 34:5 (*Polytomella*), (D) 778.54 PC 34:3 (*Polytomella*), (E) 804.55 PC 36:4 (Neurons), (F) 782.57 PC 34:1(Neurons). Precursor ions are marked by a blue diamond.

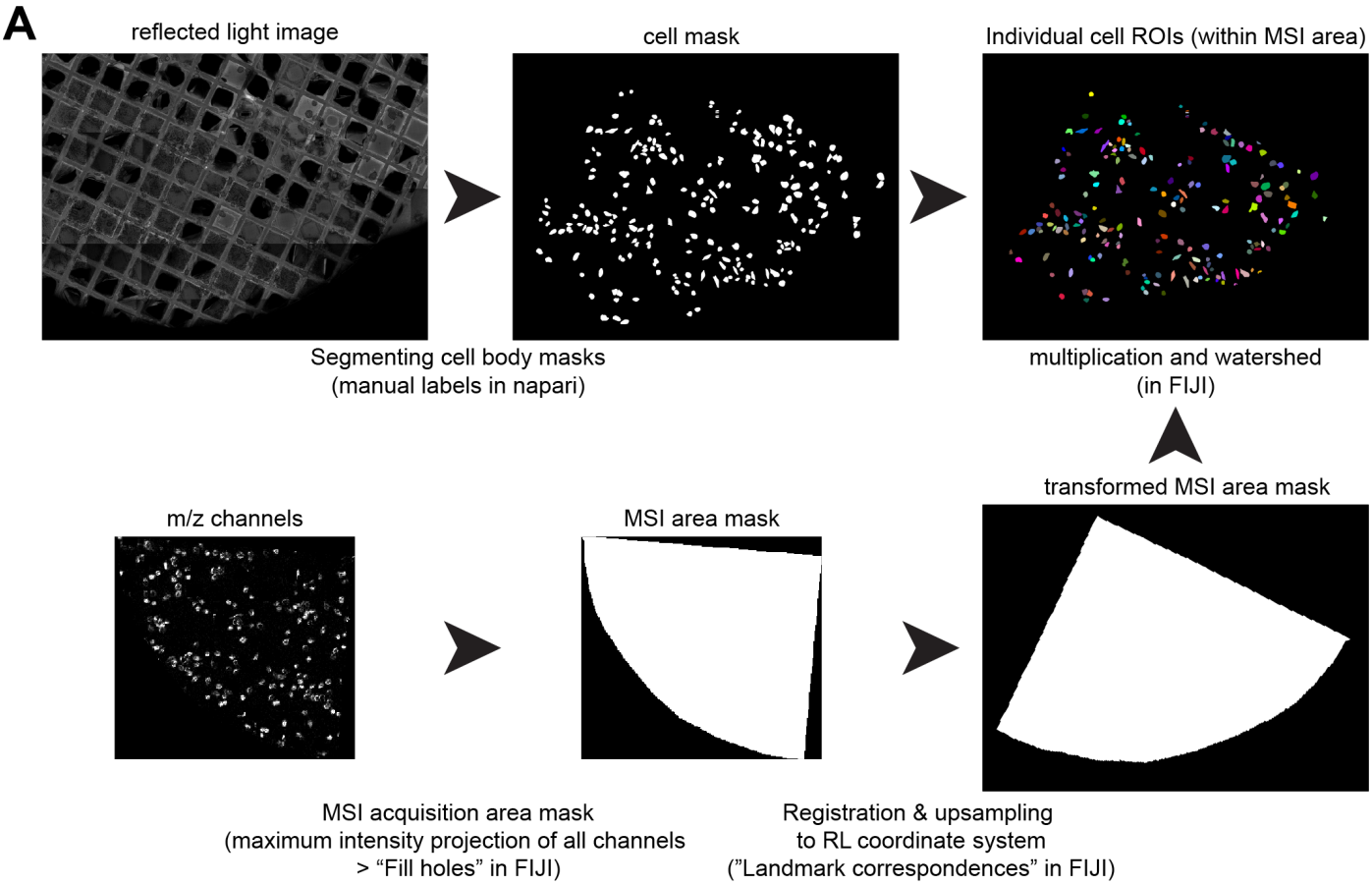

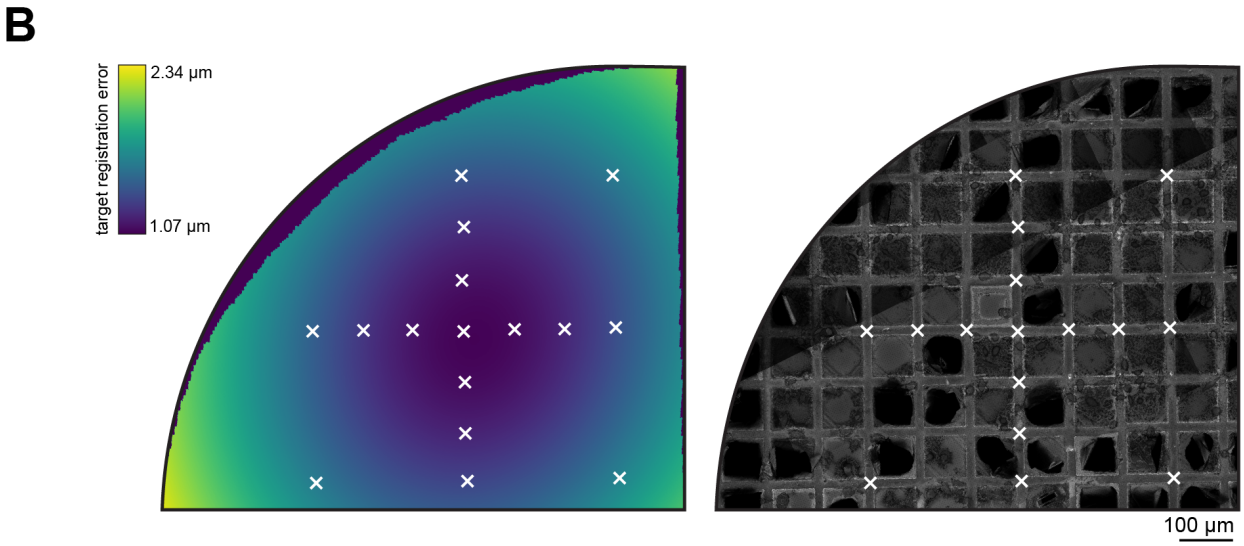

Figure S4: HeLa grid registration error estimation and cell mask creation. (A) Target registration error estimation as calculated for mass spectrometry imaging (MSI) to reflected light (RL) registration based on displayed landmark points, color-coded in viridis. Pixel size of MSI = 5 μm, reflected light = 0.33 um. **(B)** Cell mask generation for HeLa grid. Individual cell masks were manually created from RL image. A MSI area mask was created via maximum intensity projection of all MSI channels and registered with landmark points displayed in (A). Images were multiplied and single cell masks generated via watershed.

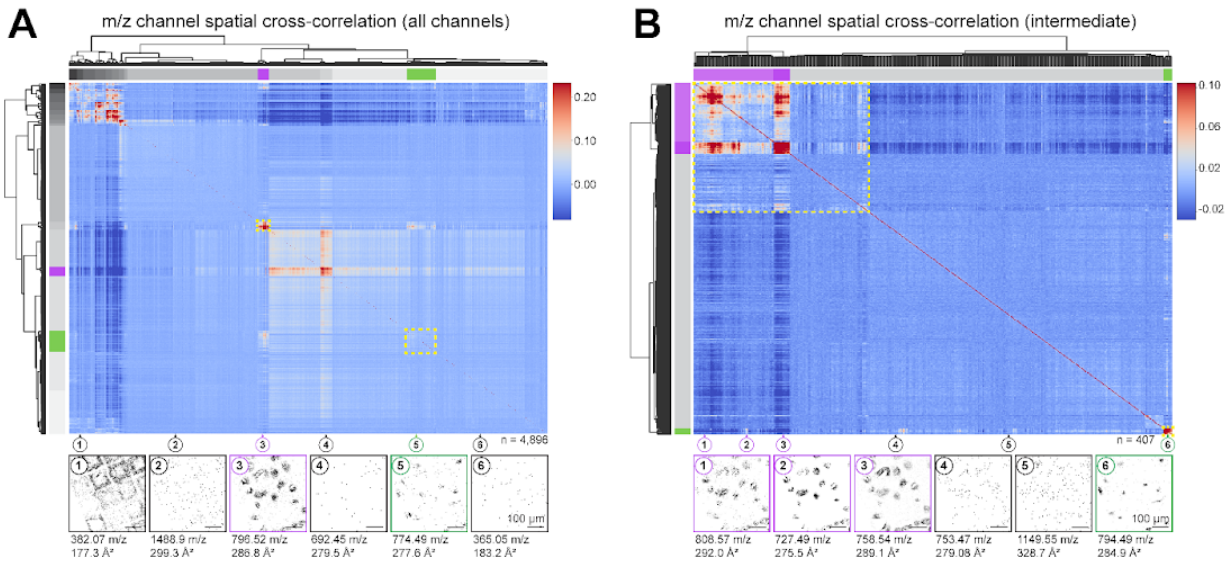

Figure S5: Pre-filtering of cell-specific m/z channels via hierarchical clustering of normalized spatial correlations of mixed HeLa/*Polytomella* grid. (A) Level 1: All m/z channels (n=4,896). Clusters containing cell-specific channels are highlighted in green (*Polytomella*) and magenta (HeLa). Example m/z channels for selected clusters are shown. **(B)** Level 2: Second round of clustering with extracted m/z channels from (A). Channels with poor signal-to-noise ratio are removed, highlighted clusters are designated as cell-specific and used in Fig 3A (n=407).

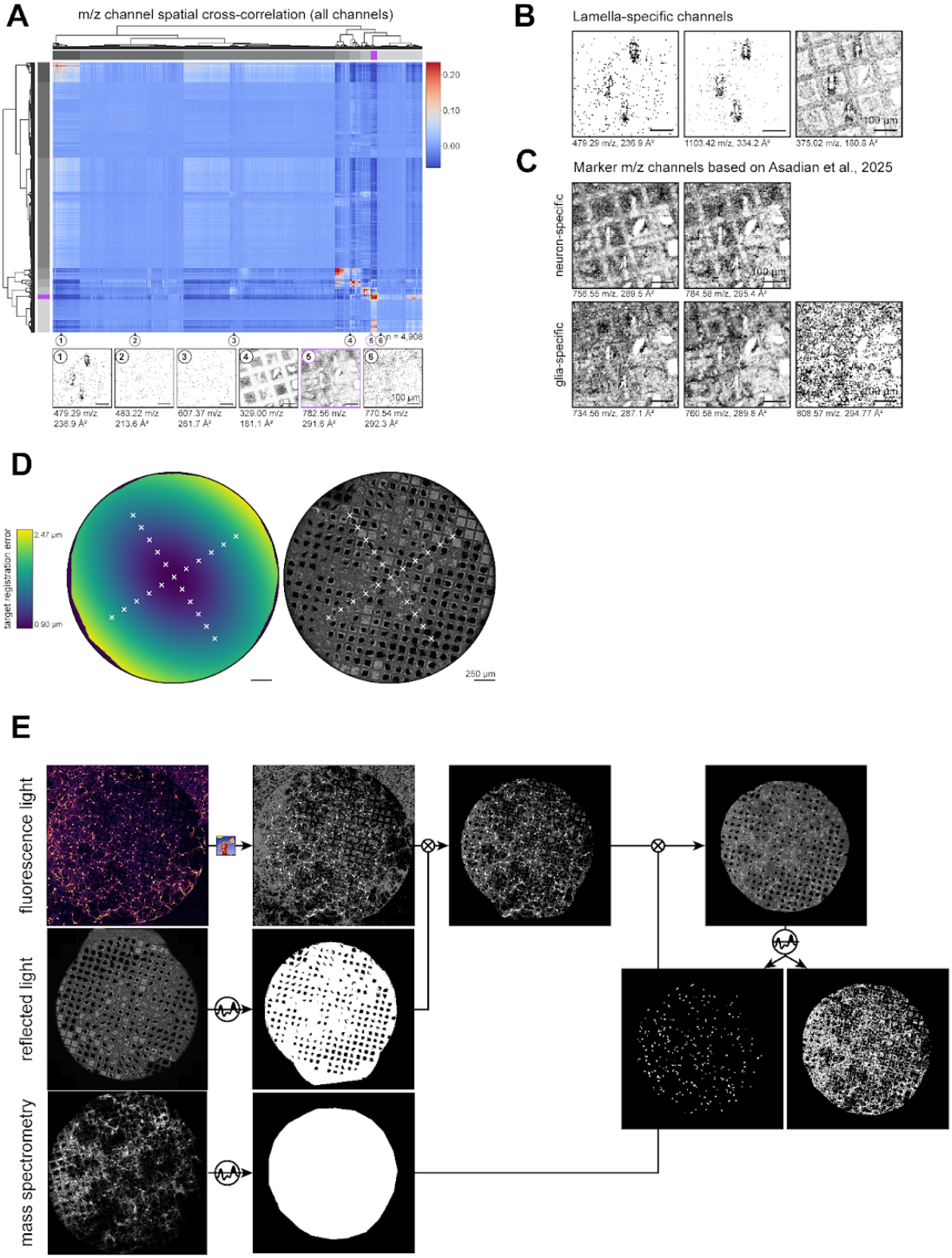

Figure S6: Pre-filtering of cell-specific channels, examples of lamella-enriched and marker channels, registration error estimation, and mask creation of neuron grid. (A) Pre-filtering of cell-specific m/z channels via hierarchical clustering of normalized spatial correlations of neuron grid. All m/z channels (n=4,908). Clusters containing cell-specific channels are highlighted in magenta. Example m/z channels for selected clusters are shown. **(B)** Some m/z channels display increased intensity surrounding lamellae, indicating beam-induced changes in these molecular species. **(C)** Images of neuron- and glia-enriched m/z values identified in (Asadian et al., 2025) **(D)** Target registration error estimation as calculated for mass spectrometry imaging (MSI) to reflected light registration based on displayed landmark points, color-coded in viridis. Pixel size of MSI = 5 um, reflected light = 0.33 um. **(E)** Soma/neurite mask generation for neuron grid. Initial soma/neurite segmentation was performed on NeuO fluorescence light image via neural network-based pixel classification. A grid defect mask was created based on the reflected light image, registered using landmark points in (D), and multiplied with the soma/neurite mask. A final mask marking the MSI acquisition area was created by maximum intensity projection of all m/z channels, registered, and also multiplied to create the final soma/neurite mask. Soma and neurite masks were applied separately for m/z intensity measurements.